PAPER

Check for updates

Studies on the optical stability of CsPbBr₃ with different dimensions (0D, 1D, 2D, 3D) under thermal environments†

Jindou Shi, [ID] [a] Minqiang Wang,*[a] Zheyuan Da,[a] Chen Zhang,[a] Junnan Wang,[a] Yusong Ding,[a] Youlong Xu [ID] *[a] and Nikolai V. Gaponenko[b]

The thermal stability of phosphor materials had long been a bottleneck in their commercialization. Nowadays, cesium lead halide perovskite CsPbBr₃ has been considered a potential replacement for the next generation of optoelectronic devices due to its excellent optical and electronic properties, however, the devices inevitably generate high temperatures on the surface under prolonged energization conditions in practical applications, which can be fatal to CsPbBr₃. Despite the various strategies that have been employed to improve the thermal stability of CsPbBr₃, systematic studies of the thermal stability of the basis CsPbBr₃ are lacking. In this study, CsPbBr₃ with different dimensions (0D quantum dots (QDs), 1D nanowires (NWs), 2D nanoplate (NPs), 3D micron crystals (MCs)) was prepared by traditional high-temperature thermal injection, and a systematic study was carried out on their optical properties and thermal stability. The results revealed that the dimensional change will directly influence the optical properties as well as the thermal stability of CsPbBr₃. In particular, 3D CsPbBr₃ MCs maintained relatively high thermal stability under high-temperature environments, which will bring interest for the commercialization of next-generation perovskite optoelectronic devices.

Introduction

In recent years, cesium lead halide perovskite materials CsPbBr₃ have received widespread attention for their excellent optical and electronic properties, which have been successfully applied in the fields of light-emitting diodes, solar cells, and photodetectors.[1–5] Unfortunately, the instability of CsPbBr₃ under multiple environments (thermal, moisture, light) prevented their further commercial development, significantly limiting practical applications.[6,7] Especially, the optical stability of CsPbBr₃ under thermal environment has been most important, which mainly stemmed from the fact that optoelectronic devices inevitably generated high temperatures on the device surface during long-term energized conditions, thereby placing a high demand on the optical stability of CsPbBr₃.[8–12] However, the soft matter structure of CsPbBr₃ enables them to exhibit a strong response to small perturbations of the external thermal environment,[13] which would be highly unfavorable to the development of perovskite optoelectronic devices; thus, it is urgent to systematically investigate the optical stability of CsPbBr₃ under thermal environments.

Currently, the research on the thermal stability of CsPbBr₃ is mainly concentrated on surface modification and ion doping strategies to enhance its optical stability under a thermal environment.[13–15] For example, the surface encapsulation of CsPbBr₃ nanocrystals (NCs) by an organic polymer thermoplastic polyurethane (TPU) lowered the fluorescence loss ratio of CsPbBr₃ NCs under a high-temperature environment.[16] Highly stable ZrO₂ was employed to provide a surface coating on CsPbBr₃ NCs, enhancing their thermal stability and ensuring their luminescent efficiency under high temperatures.[17] Moreover, the F ion doping effectively suppressed the fluorescence quenching of CsPbBr₃ NCs under high temperatures, thereby guaranteeing the stable operation of the optoelectronic device.[18] It can be seen that thermal stability studies for CsPbBr₃ have been carried out mainly around post-treatment strategies, with little research on the key material CsPbBr₃, which would be not conducive to subsequent selection for commercial preparation.[19–21]

Herein, CsPbBr₃ with different macroscopic dimensions (0D quantum dots (QDs), 1D nanowires (NWs), 2D nanoplate

[a]Electronic Materials Research Laboratory, Key Laboratory of the Ministry of Education International Center for Dielectric Research & Shannxi Engineering Research Center of Advanced Energy Materials and Devices, Xi'an Jiaotong University, 710049 Xi'an, China. E-mail: mqwang@xjtu.edu.cn
[b]Belarusian State University of Informatics and Radioelectronics, P. Browki 6, 220013 Minsk, Belarus
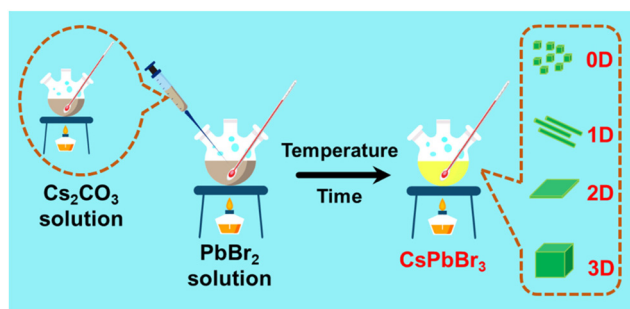†Electronic supplementary information (ESI) available. See DOI: https://doi.org/10.1039/d3nr01863f

Fig. 1 Schematic representation of the preparation for $CsPbBr_3$ with different dimensions (0D, 1D, 2D, 3D).

(NPs), 3D micron crystals (MCs)) was prepared to investigate their optical stability under high-temperature environments (Fig. 1), thereby, selecting the stable core material $CsPbBr_3$ from the source. Firstly, the traditional thermal injection method was applied to obtain $CsPbBr_3$ with different dimensions by adjusting the ratio of precursors and controlling the reaction temperature and time. Subsequently, the optical properties of $CsPbBr_3$ with different dimensions and their stability under thermal environments were thoroughly investigated. The results show that 0D $CsPbBr_3$ QDs have the highest photoluminescence quantum yields (PLQYs) at room temperature, but they are most unstable at high temperatures, with rapid fluorescence quenching. In contrast, the larger volume of 3D $CsPbBr_3$ MCs allowed them to exhibit more stable optical emission when exposed to external thermal environments, although their optical properties at room temperature were slightly inferior, which does not hinder the prospects for applications in optoelectronics. Therefore, $CsPbBr_3$ with different

dimensions has its own advantages and disadvantages, which need to be selected according to the different application environments. This report will contribute to a systematic reference for the commercial selection in the preparation of $CsPbBr_3$ optoelectronic devices, thereby, further broadening the sustainable development of perovskites in the future optoelectronic market.

Results and discussion

0D $CsPbBr_3$ QDs, 1D $CsPbBr_3$ NWs, 2D $CsPbBr_3$ NPs, and 3D $CsPbBr_3$ MCs were prepared by tightly controlling the proportion of the reaction precursors as well as the reaction conditions during high-temperature thermal injection. The TEM image (Fig. 2a) showed that the average particle size of the $CsPbBr_3$ QDs was 8 nm, which is approximately equal to its excitonic Bohr radius (7 nm) and belongs to a typical macroscopic 0D structure that will exhibit strong quantum confinement effects.[22] Clear lattice stripes were observed on the corresponding HRTEM image (Fig. 2e), indicating that the 0D $CsPbBr_3$ QDs possess a decent crystallinity and that the lattice spacing on the crystal surface was 0.42 nm, which corresponded exactly to the (020) crystal plane of orthorhombic $CsPbBr_3$. Furthermore, the energy dispersive spectroscopy (EDS) elemental mapping spectrum (Fig. S1a and e†) was analyzed for their corresponding elemental distribution and the results showed that Cs, Pb, and Br presented a uniform distribution in the crystals. Finally, the crystal structure of 0D $CsPbBr_3$ QDs was further studied by XRD (Fig. 2i), and the pattern showed that all the diffraction peaks of $CsPbBr_3$ QDs matched perfectly with the bottom reference orthorhombic
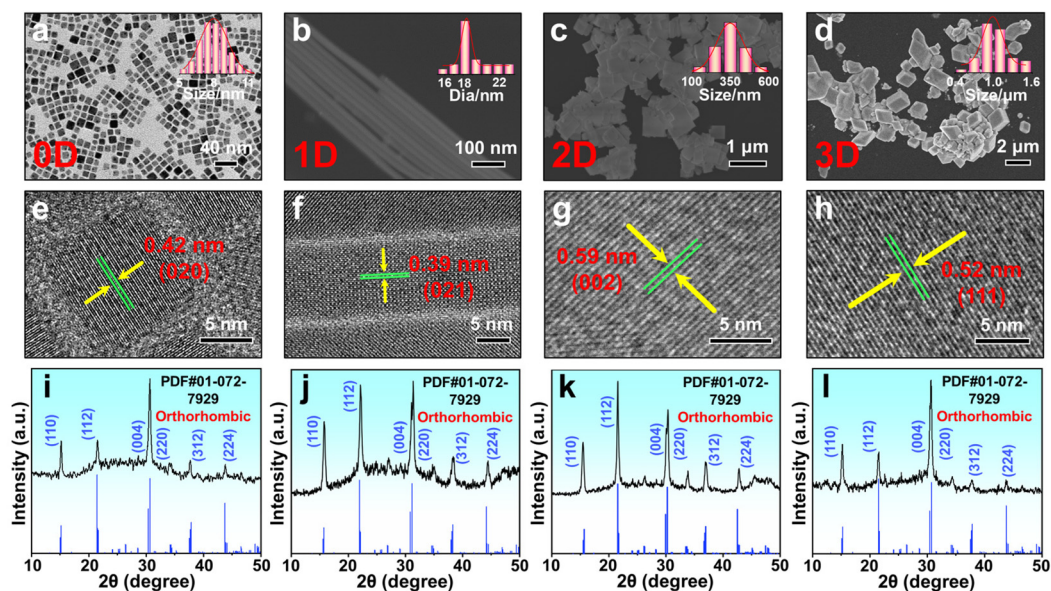

Fig. 2 TEM (transmission electron microscope) image of 0-dimensional (0 D) $CsPbBr_3$ QDs (a), scanning electron microscope (SEM) images of 1D $CsPbBr_3$ NWs (b), 2D $CsPbBr_3$ NPs (c), and 3D $CsPbBr_3$ MCs (d). Corresponding high-resolution transmission electron microscopy (HRTEM) images (e–h) and X-ray diffraction (XRD) patterns (i–l) of different samples.

CsPbBr$_3$ (Powder Diffraction File (PDF): 01-072-7929, space group: *Pbnm* (62)) and no other impurity phases were detected,[23] indicating that pure phases of 0D CsPbBr$_3$ QDs were obtained. In some previous studies, it was found that 2D NPs were easily generated during the synthesis of 0D CsPbBr$_3$ QDs,[24] which was completely overcome in this report by adjusting the ratio of the reaction precursors, thereby ensuring the purity of 0D CsPbBr$_3$ QDs. As can be seen from the SEM image of CsPbBr$_3$ NWs (Fig. 2b), the obtained CsPbBr$_3$ NWs exhibited an extremely high aspect ratio, with the average diameter of the crystal being only 18 nm, but the corresponding lengths are in the micrometer scale, which belongs to a typical 1D wire structure, and the three elements (Cs, Pb, Br) were uniformly distributed in the wires (Fig. S1b and f†). The lattice stripes of each NWs are clearly visible (Fig. 2f), with the middle CsPbBr$_3$ NWs having a lattice spacing of 0.39 nm, corresponding to the (021) crystal plane of the orthorhombic CsPbBr$_3$. The XRD pattern showed that the crystal structure corresponding to CsPbBr$_3$ NWs remained in the orthorhombic phase as the dimensions changed (Fig. 2j). Additionally, 2D CsPbBr$_3$ NPs with an average size of 250 (Fig. 2c) and a thickness of about 40–70 nm (Fig. S2†) were obtained by adjusting the reaction conditions, and all elements are neatly distributed on the plate (Fig. S1c and g†). The perfect crystallinity of the NPs was facilitated by the prolonged reaction time at high temperatures, and the lattice striations on the crystal surface are obvious, corresponding to the (110) crystal plane of orthorhombic CsPbBr$_3$ (Fig. 2g), which also belongs to the space group *Pbnm* (62). The XRD pattern reveals no appearance of an additional second phase in the 2D CsPbBr$_3$ NPs, matching it exactly to the reference orthorhombic CsPbBr$_3$ (PDF: 01-072-7929) below (Fig. 2k), which means that the pure phase of CsPbBr$_3$ NPs was successfully prepared. Meanwhile, the 3D CsPbBr$_3$ MCs were already grown to the micron scale, which is inextricably linked to the controlled reaction conditions, and its average size was maintained at around 1 μm (Fig. 2d). Similarly, the well-defined lattice striations on the surface reflect its excellent crystallinity and the lattice spacing is 0.52 nm, corresponding to the (111) crystal plane of orthorhombic CsPbBr$_3$ (Fig. 2h). As can be seen from the elemental mapping spectrum (Fig. S1d and h†), the distribution of elements Cs, Pb and Br was detected in CsPbBr$_3$ MCs, which further confirmed the fact that 3D CsPbBr$_3$ MCs were synthesized. The detected XRD diffraction peaks (Fig. 2l) indicate that the 3D MCs are also orthorhombic structures and belong to the space group *Pbnm* (62).[25] The analysis of the results indicated that the macroscopic dimensional changes in the CsPbBr$_3$ crystals did not induce a transformation of the crystal structure, which remained in the orthorhombic phase, a similar phenomenon also observed in previous reports.[26] It has been demonstrated that the modulation of the morphology of CsPbBr$_3$ crystals can be achieved by a simple high-temperature thermal injection method, laying the foundation for subsequent research into the link between their morphology and optical properties.

The optical properties of CsPbBr$_3$ with different dimensions (0D, 1D, 2D, and 3D) were further investigated to analyze the impact of their macroscopic morphology on the optical behaviors. The PL spectra of CsPbBr$_3$ with different dimensions (0D, 1D, 2D, and 3D) showed that all the fluorescence emission peaks were concentrated at 510–530 nm (Fig. 3a), which belonged to the green region of visible light, indicating that they could be applied as green light sources in photoelectric devices. In particular, the corresponding PL emission peaks displayed a red-shift as the macroscopic dimension of CsPbBr$_3$ increased, which was attributed to the quantum confinement effect of CsPbBr$_3$, with the energy band gap following the change in volume, as has been reported in other materials.[27,28] Subsequently, the absorbance spectra of CsPbBr$_3$ with different dimensions displayed their absorption edge concentrated in the region of 500–530 nm, as well as a red shift with increasing volume, corresponding exactly to their PL emission peaks (Fig. 3b). From the band gap fitting of the samples, it can be seen that the energy band gap gradually narrowed from 2.39 eV of 0D CsPbBr$_3$ QDs to 2.37 of 3D CsPbBr$_3$ MCs, which again confirmed that the optical properties of CsPbBr$_3$ were modulated by the macroscopic dimension. However, the small range of variation in the band gap can be attributed mainly to the fact that the size of the samples was larger than the excitonic Bohr radius of CsPbBr$_3$, resulting in a weaker quantum confinement effect on the band structure.[29] Moreover, the time-resolved PL decay behavior of CsPbBr$_3$ with different dimensions was recorded, allowing for deeper insight into the influence of dimensional changes on the carrier dynamics of CsPbBr$_3$ powder (Fig. 3c). The fitting results indicated that the PL decay curves of all samples followed a double exponential decay function (Table S1†), where the fast decay lifetime (τ_1) was associated with trap-assisted recombination within CsPbBr$_3$, and the slow decay lifetime (τ_2) was derived from the radiative recombination of excitons.[30,31] On the other hand, the radiative recombination ratio (A_2) in 0D CsPbBr$_3$ QDs was up to 61.5%, implying that more excitons undergo radiative recombination, thereby releasing more photons. In contrast, the trap-assisted recombination ratio (A_1) of 3D CsPbBr$_3$ MCs reached 57.2%, which can be attributed to the slow crystallization process of MCs under a high-temperature environment, increasing its internal defective states.[32,33] Meanwhile, the radiative recombination ratios (A_2) for 1D CsPbBr$_3$ NWs and 2D CsPbBr$_3$ NPs were 58.7% and 53.9% respectively, which were positively correlated with their crystallization times. Finally, the CsPbBr$_3$ with different dimensions emitted bright green light under a 365 nm UV light (Fig. 3d), which corresponded to the results shown in their PL spectra. Unfortunately, the PLQY values of CsPbBr$_3$ varied with their macroscopic dimensions, which can mainly stem from differences in the radiative recombination ratios of their internal excitons,[34] in addition to the reabsorption of the emitted light by large-sized crystals, such that 0D CsPbBr$_3$ QDs exhibited the strongest fluorescence emission (PLQYs of 86%), while 3D CsPbBr$_3$ MCs had the weakest fluorescence emission (PLQYs of 72%). Based on the above comparison, it can be concluded
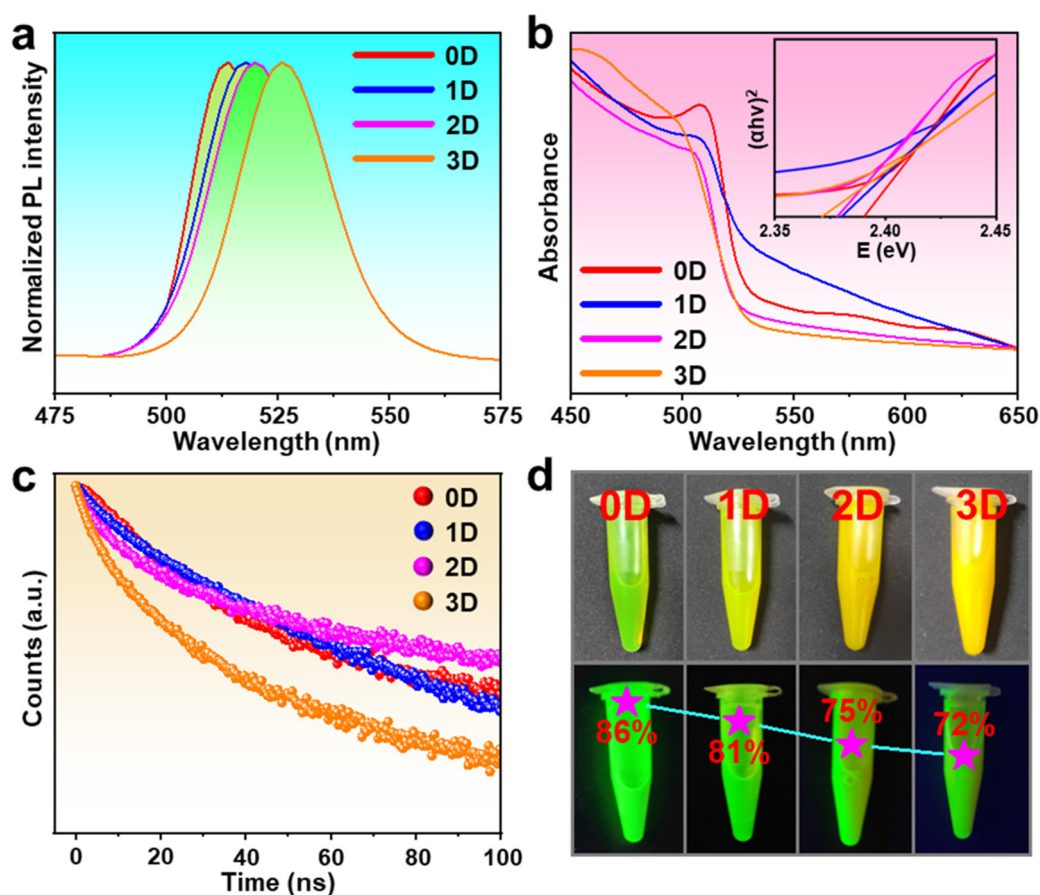
Fig. 3 Normalized PL spectra (a), absorption spectra (b), and time-resolved PL spectra (c) of CsPbBr$_3$ with different dimensions (0D, 1D, 2D, and 3D). Photographs and PLQYS values (d) of samples under daylight (top) and 365 nm UV light (bottom). Insets in (b) show the corresponding $(\alpha h\nu)^2$ *vs.* photon energy (eV) curves of different samples.

that the macroscopic dimensional variations of CsPbBr$_3$ can directly affect their optical properties, but the optical stability of CsPbBr$_3$ under high-temperature environments will be more important in practical applications, as optoelectronic devices will inevitably generate high temperatures after prolonged energization, which can be fatal to the loss of fluorescent materials. At the same time, the large particle size of 3D CsPbBr$_3$ MCs resulted in the inability to form high-quality and uniform films. In the subsequent study, the focus was on the optical stability of CsPbBr$_3$ powder with different dimensions under different thermal environments.

It is well known that metal halide perovskites belong structurally to the class of soft matter systems and therefore CsPbBr$_3$ will exhibit a large response in dealing with changes in ambient temperature,[35] which has become a stumbling block in its practical applications.[13] Subsequently, heating–cooling cycle tests at 373 K were carried out separately for CsPbBr$_3$ with different dimensions (0D, 1D, 2D, and 3D) in order to analyze the relationship between the macroscopic dimensions and their thermal stability. It can be clearly seen that all CsPbBr$_3$ exhibited varying degrees of fluorescence quenching with increasing ambient temperature (Fig. 4a–d),

followed by a gradual recovery of fluorescence intensity as the temperature decreases to room temperature (Fig. 4e–h). Not only that, all samples showed a blue shift in the position of the PL emission peak when the ambient temperature was increased and gradually returned to the initial position during the subsequent cooling down. This blueshift of the PL emission peak was caused by the out-of-phase band-edge states stabilized as lattice dilation at the Brillouin zone boundary, and has been reported previously in organometal halide perovskite materials.[36–38] It is pleasing to note that the exciton binding energy (E_a) of inorganic materials has become a standard for assessing the thermal stability of materials, and the Arrhenius equation was proposed to be applied to fit the relationship between PL intensity and temperature change to determine E_a values for CsPbBr$_3$ with different dimensions (insets in Fig. 4a–d).[3,18]

$$I(T)=\frac{I_0}{1+A\mathrm{e}^{-E_a/(\kappa T)}} \qquad (1)$$

where $I(T)$ and I_0 are the PL intensity at different temperatures and the initial PL intensity, respectively, A is a constant parameter, and κ is the Boltzmann constant (8.629×10^{-5} eV K^{-1}).
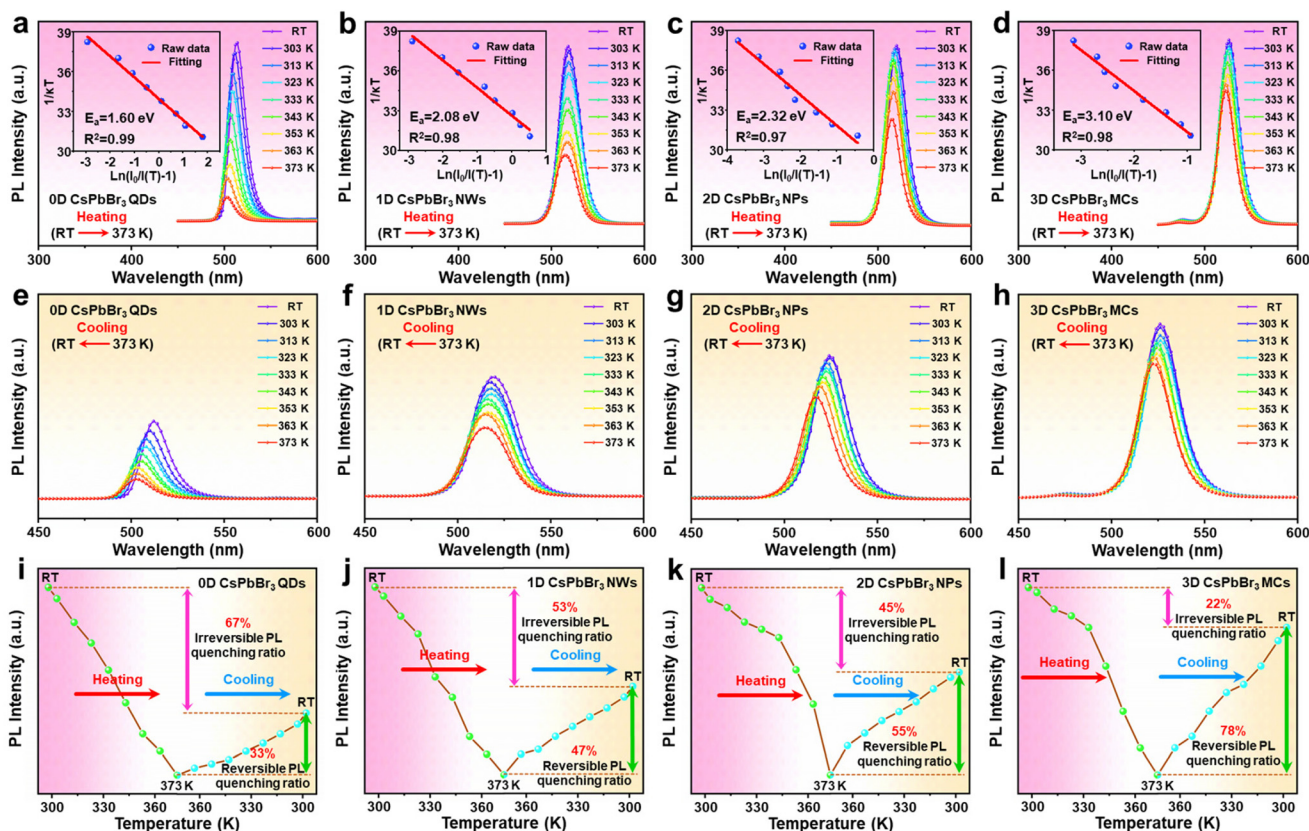
Fig. 4 PL spectra of CsPbBr$_3$ with different dimensions (0D, 1D, 2D and 3D) during heating (a–d) and cooling (e–h) cycles at 373 K, corresponding to the analysis of the relative change in PL intensity (i–l). Insets in (a–d) are the relationship between ln($I_0/I(T) - 1$) versus $1/\kappa T$ for the different samples, respectively.

As can be seen from the results, the E_a value of CsPbBr$_3$ gradually improves as the dimensionality increases, with 0D, 1D, 2D, and 3D corresponding to 1.60 eV, 2.08 eV, 2.32 eV, and 3.10 eV, respectively. The analysis of the results leads to the conclusion that the boost in exciton energy is inextricably linked to the shift in the macroscopic dimension of CsPbBr$_3$. In particular, the larger surface area of the 0D CsPbBr$_3$ QDs allows for an elevated rate of heat exchange with them under high-temperature conditions, resulting in lower thermal resistance, while the 3D CsPbBr$_3$ MCs benefits from their large volume and small surface area, allowing them to show a smaller response in dealing with the external thermal environment. Unfortunately, the PL intensities of CsPbBr$_3$ with different dimensions could not be restored to their initial intensities during the subsequent cooling down, although the temperature had by then returned to room temperature. Where the part of the PL intensity recovered during the cooling process was defined as reversible fluorescence quenching, and the difference between the final state and the initial PL intensity was defined as irreversible fluorescence quenching, the two thermal behaviors are related to the two different types of trap states produced by thermal activation. Especially, thermally-induced permanent crystal structure changes produce trap states that cannot be eliminated, thereby triggering irreversible
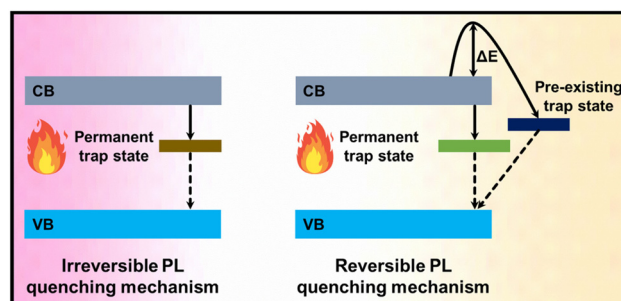
fluorescence quenching (Fig. 5 left). At the same time, the "soft" lattice and lower defect formation energy of cesium lead halide perovskites can introduce relatively large defect concentrations, and imperfect lattices such as point defects will induce pre-existing trap states.[39,40] Therefore, reversible fluorescence quenching can be attributed to either the thermally activated escape of carriers to pre-existing (surface) trap states and/or the thermally activated creation of temporary trap states, which relax upon cooling (Fig. 5 right).[41] It is striking

Fig. 5 Mechanisms of irreversible (left) and reversible (right) fluorescence quenching.

that the $CsPbBr_3$ with different dimensions also show significant differences in PL intensity recovery during cooling, with 3D $CsPbBr_3$ MCs showing higher PL intensity recovery, which also implies that it produces fewer permanent defects under thermal conditions, 0D $CsPbBr_3$ QDs doing exactly the opposite, and 1D $CsPbBr_3$ NWs and 2D $CsPbBr_3$ NPs being in the middle of the range. Lastly, the reversible and irreversible PL quenching ratios were introduced to further analyze the defect generation modes of $CsPbBr_3$ with different dimensions during the heating–cooling cycle (Fig. 4i–l).[17]

$$\text{Irreversible PL quenching ratio} = \frac{I_i - I_r}{I_i - I_h} \quad (2)$$

$$\text{Reversible PL quenching ratio} = 1 - \text{irreversible PL quenching ratio} \quad (3)$$

where I_i, I_r, and I_h are the PL intensity at initial room temperature, the PL intensity after cycling back to room temperature, and the PL intensity when heated to the maximum temperature (373 K), respectively. It was calculated that when the macroscopic morphology of $CsPbBr_3$ was changed from 0D to 3D, the irreversible PL quenching ratio of the corresponding sample decreased from 67% to 22% and the reversible fluorescence quenching ratio showed a corresponding improvement (from 33% to 78%), which again indicated that only a small percentage of permanent defect states were produced in the 3D $CsPbBr_3$ MCs during the heating process. From the above analysis of the PL intensity changes during the heating and cooling cycles of $CsPbBr_3$ with different dimensions (0D, 1D, 2D, and 3D), it is clear that 3D $CsPbBr_3$ MCs exhibit excellent thermal stability, which is particularly important in the commercial development process of $CsPbBr_3$.

For insight into the thermal environmental influences on the stability of $CsPbBr_3$ with different dimensions (0D, 1D, 2D, and 3D), the variations in their structural and optical behavior over time under different annealing temperatures (333 K and 373 K) were investigated. The results showed that $CsPbBr_3$ with different dimensions exhibited secondary growth after being stored at high temperatures for 20 min, and the signal of maturation was more intensified as the temperature increased (Fig. 6). This phenomenon was attributed to oleic acid (OA) and oleyl amine (OAm) ligands on the surface of $CsPbBr_3$ being mixed to form new ammonium carboxylate ligands under a high-temperature environment, which induced different intensities of Ostwald ripening effect at different temperatures (333 K and 373 K),[42] so that the regrowth of $CsPbBr_3$ particle size was observed (Fig. 6a–h), corresponding to an improvement in crystalline intensity (Fig. 6i–l). At the same time, the optical properties of $CsPbBr_3$ with different dimensions (0D, 1D, 2D, and 3D) were noticeably affected, with all samples displaying a red shift in the PL emission peaks, which were directly associated with the grain size being increased. Especially, the PL emission peak of 0D $CsPbBr_3$ QDs showed the broadest red-shifted range, with 1D $CsPbBr_3$ NWs and 2D $CsPbBr_3$ NPs being relatively smaller, and the corresponding absorption peaks also exhibited different levels of shift, while their energy band gap also shrank with the temperature increasing. In striking contrast, the PL emission peak of 3D $CsPbBr_3$ MCs had a very minimal red shift with increasing temperature, and the corresponding absorption peak and energy band gap remained almost unchanged. The variations of optical behaviors mentioned above were inextricably linked to the quantum size effect of $CsPbBr_3$. When the particle sizes of $CsPbBr_3$ were smaller, the slight alteration in
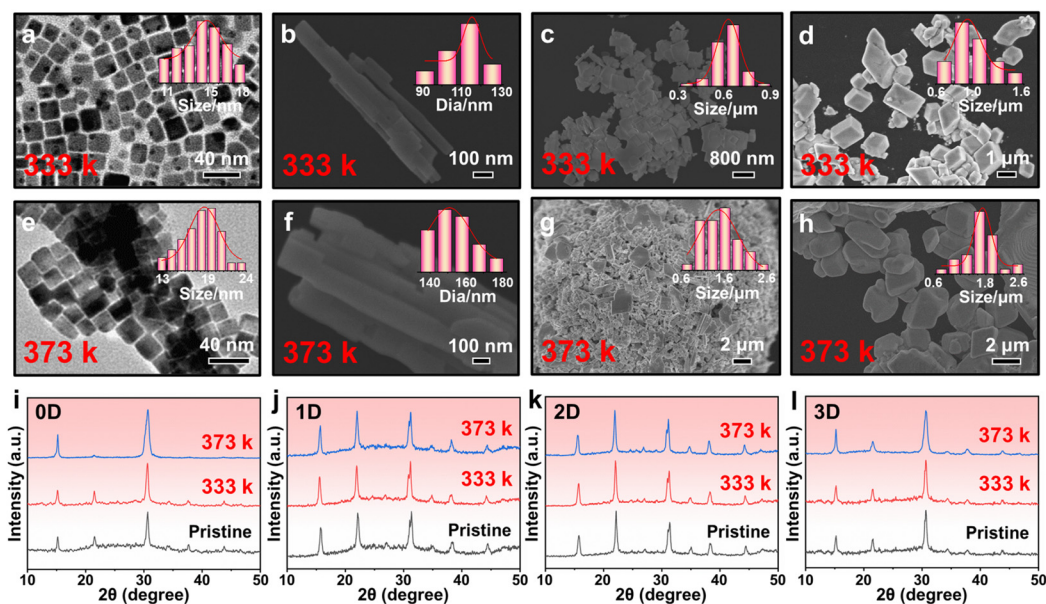

Fig. 6 TEM images of 0D $CsPbBr_3$ QDs after annealing at 333 K (a) and 373 K (e) for 20 min. SEM images of 1D $CsPbBr_3$ NWs (b and f), 2D $CsPbBr_3$ NPs (c and g), and 3D $CsPbBr_3$ MCs (d and h) after annealing at 333 K and 373 K for 20 min. XRD patterns of $CsPbBr_3$ QDs (i), $CsPbBr_3$ NWs (j), $CsPbBr_3$ NPs (k), and $CsPbBr_3$ MCs (l) at different annealing temperatures.
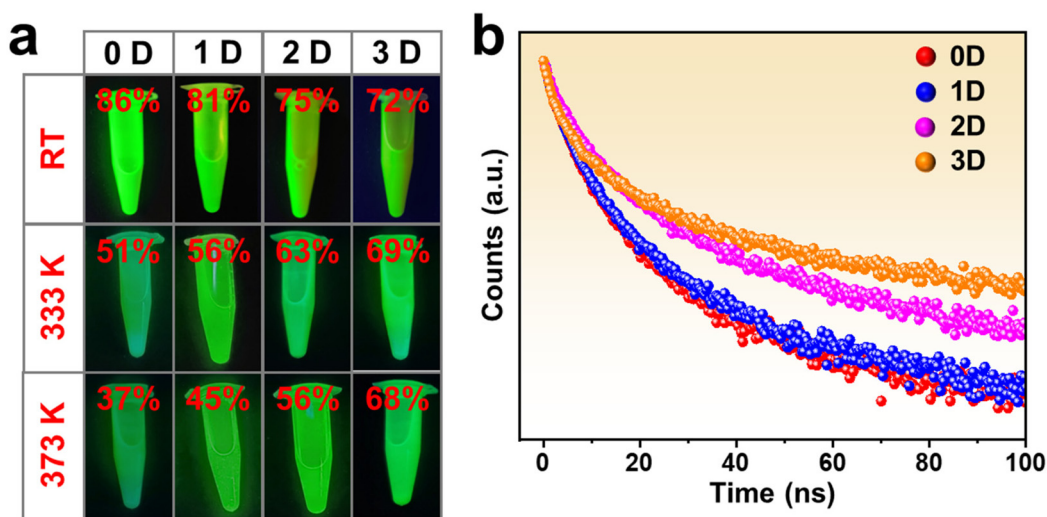
Fig. 7 (a) The fluorescence photographs and PLQYs of $CsPbBr_3$ with different dimensions (0D, 1D, 2D and 3D) after annealing at 363 K and 373 K for 20 min, respectively. (b) Time-resolved PL spectra of $CsPbBr_3$ with different dimensions (0D, 1D, 2D, and 3D) after annealing at 373 K for 20 min.

their size would directly contribute to a substantial shift in their optical behavior, resulting from the increase (or decrease) in the grain size caused the shrinkage (or broadness) of the energy band gap, corresponding to the simultaneous red-shift (or blue-shift) of PL and absorption peaks.[43,44]

Unfortunately, the PLQYs of $CsPbBr_3$ with different dimensions (0D, 1D, 2D, and 3D) decayed accompanied by increased annealing temperature, and the loss of PL intensity at this point was permanent, with no tendency for the fluorescence intensity of $CsPbBr_3$ to recover, despite the temperature has returned to room temperature (Fig. 7a). This phenomenon was associated with the two different types of trap states generated by thermal activation mentioned above, where prolonged storage of $CsPbBr_3$ in a high thermal environment resulted in aggravated thermally induced permanent crystal structure changes, which produced more permanent defect states that could not be eliminated. Of these, 0D $CsPbBr_3$ QDs showed the most marked fluorescence decay, corresponding to a reduction in PLQYs from the initial 86% to 37%. Meanwhile, 1D $CsPbBr_3$ NWs and 2D $CsPbBr_3$ NPs also exhibited varying degrees of loss of PLQYs, eventually remaining at 45% and 56%, respectively. Conversely, the performance of 3D $CsPbBr_3$ MCs was most remarkable, retaining 68% of the PLQYs after being stored at 373 K for 20 min. Subsequently, to investigate the effect of the thermal environment on the carrier dynamics of $CsPbBr_3$ with different dimensions (0D, 1D, 2D, and 3D), the time-resolved PL decay behavior of the samples was recorded separately after being stored at 373 K for 20 min (Fig. 7b). The fitting results indicated that long-term thermal environmental storage increased the ratio of non-radiative recombination in $CsPbBr_3$, which was associated with the thermally-induced generation of additional permanent trap states, making increased trap-assisted recombination, directly reflected in the fluorescence intensity decay of $CsPbBr_3$. Strikingly, the carrier radiative recombination rate of 3D

$CsPbBr_3$ MCs showed little variation, keeping it at 39.3% (compared to an initial 42.8%). However, the radiative recombination rate for 0D $CsPbBr_3$ QDs decayed devastatingly from an initial 61.5% to 29.1%, and for 1D $CsPbBr_3$ NWs and 2D $CsPbBr_3$ NPs, it dropped to 33.1% and 37.3% respectively. At the same time, the corresponding τ_{ave} of $CsPbBr_3$ with different dimensions (0D, 1D, 2D, and 3D) also attenuated, which followed the same trend as its PLQYs, of which 0D $CsPbBr_3$ MCs exhibited the highest fluorescence lifetime and PLQY. The above results revealed that the changes in the optical properties of $CsPbBr_3$ under thermal environments were all inextricably linked to the macroscopic scale, the larger surface area of the 0D QDs being more likely to be contacted with the thermal source, thereby generating more trap states, and resulting in the sacrifice of their fluorescence emission. The smaller surface area of 3D MCs demonstrated greater structural stability in responding to variations in the external thermal environment, thus maintaining a stable and efficient green fluorescence emission. Obviously, the 3D $CsPbBr_3$ MCs with large volumes maintained high structural stability under thermal environments, thereby effectively overcoming the fluorescence decay phenomenon, greatly enhancing its future competitiveness in the perovskite lighting market. Despite the poor film-forming properties of 3D $CsPbBr_3$ MCs, it can be mixed with the polymer in practice to obtain the uniform film,[17] which can be assembled with InGaN chips to form stable optoelectronic devices.

Conclusions

In summary, $CsPbBr_3$ with different dimensions (0D, 1D, 2D, 3D) were prepared by adjusting the ratio of precursors, controlling the reaction time and temperature, then their optical properties, as well as their optical stability under a high-tempera-

ture environment, were investigated. Unfortunately, 0D CsPbBr$_3$ QDs generated a large number of permanent trap states within them under a high-temperature environment that could not be eliminated, resulting in irreversible quenching of their optical properties. The improved thermal stability of 1D CsPbBr$_3$ NWs and 2D CsPbBr$_3$ NPs were closely related to the change in their dimensions, where the decreased relative surface area allowed for a reduced probability of interaction with the external thermal environment, thereby preserving the optical stability. In stark contrast, 3D CsPbBr$_3$ MCs showed excellent optical stability under a high-temperature thermal environment, which was attributed to their smallest relative surface area, and the disturbance of the external thermal environment did not induce the generation of massive trap states, ensuring the stability of the PL emission. In addition, the film formation technology of 3D CsPbBr$_3$ MCs also needs to be further explored to ensure that it would serve opto-electronic devices well. We believe that the outstanding thermal stability of 3D CsPbBr$_3$ MCs will provide an option for the development of stability enhancement strategies in perovskite materials, which will further widen the development path for the commercial optoelectronics market.

Author contributions

Jindou Shi: conceptualization (lead), investigation (lead), methodology (lead), writing – original draft preparation (lead); Minqiang Wang: conceptualization (equal), funding acquisition (lead), writing – review & editing (lead); Zheyuan Da: investigation (equal); Chen Zhang: investigation (equal); Junnan Wang: conceptualization (equal); Yusong Ding: investigation (equal); Youlong Xu: investigation (equal); Nikolai V. Gaponenko: investigation (equal).

Conflicts of interest

There are no conflicts of interest to declare.

Acknowledgements

References

1 J. J. Zhang, L. X. Wang, C. H. Jiang, B. Cheng, T. Chen and J. G. Yu, *Adv. Sci.*, 2021, **8**, 2102648.

2 Q. H. Mo, C. Chen, W. S. Cai, S. Y. Zhao, D. D. Yan and Z. G. Zang, *Laser Photonics Rev.*, 2021, **15**, 2100278.

3 J. D. Shi, W. Y. Ge, Y. Tian, M. M. Xu, W. X. Gao and Y. T. Wu, *Small*, 2021, **17**, 2006568.

4 H. X. Wang, P. F. Zhang and Z. G. Zang, *Appl. Phys. Lett.*, 2020, **116**, 162103.

5 J. L. Peng, C. Q. Xia, Y. L. Xu, R. M. Li, L. H. Cui, J. K. Clegg, L. M. Herz, M. B. Johnston and Q. Q. Lin, *Nat. Commun.*, 2021, **12**, 1531.

6 W. C. Xiang, S. Z. Liu and W. Tress, *Energy Environ. Sci.*, 2021, **14**, 2090–2113.

7 H. Huang, M. I. Bodnarchuk, S. V. Kershaw, M. V. Kovalenko and A. L. Rogach, *ACS Energy Lett.*, 2017, **2**, 2071–2083.

8 J. H. Ji, G. Jo, J. G. Ha, S. M. Koo, M. Kamiko, J. Hong and J. H. Koh, *J. Nanosci. Nanotechnol.*, 2018, **18**, 6029–6032.

9 Z. Sun, D. M. Wu, Y. J. Zhang, J. Zhuang and K. F. Deng, *Key Eng. Mater.*, 2012, **503**, 397–401.

10 X. Y. Lu, T. C. Hua and Y. P. Wang, *Microelectron. J.*, 2011, **42**, 1257–1262.

11 X. W. Chang, W. P. Li, L. Q. Zhu, H. C. Liu, H. F. Geng, S. S. Xiang, J. M. Liu and H. N. Chen, *ACS Appl. Mater. Interfaces*, 2016, **8**, 33649–33655.

12 Y. C. Fan, X. Y. M. Dong, Y. C. Guo, H. H. Xing, H. Y. Xia, J. Li and E. K. Wang, *Anal. Chem.*, 2022, **94**, 11360–11367.

13 B. Conings, J. Drijkoningen, N. Gauquelin, A. Babayigit, J. D'Haen, L. D'Olieslaeger, A. Ethirajan, J. Verbeeck, J. Manca, E. Mosconi, F. De Angelis and H. G. Boyen, *Adv. Energy Mater.*, 2015, **5**, 1500477.

14 T. T. Xuan, X. F. Yang, S. Q. Lou, J. J. Huang, Y. Liu, J. B. Yu, H. L. Li, K. L. Wong, C. X. Wang and J. Wang, *Nanoscale*, 2017, **9**, 15286–15290.

15 D. D. Yan, S. Y. Zhao, Y. B. Zhang, H. X. Wang and Z. G. Zang, *Opto-Electron. Adv.*, 2022, **5**, 200075.

16 J. D. Shi, W. Y. Ge, W. X. Gao, M. M. Xu, J. F. Zhu and Y. X. Li, *Adv. Opt. Mater.*, 2020, **8**, 1901516.

17 J. D. Shi, M. Q. Wang, H. Wang, C. Zhang, Y. Q. Ji, J. N. Wang, Y. Zhou and A. S. Bhatti, *Nanoscale*, 2022, **14**, 16548–16559.

18 M. M. Liu, Q. Wan, H. M. Wang, F. Carulli, X. C. Sun, W. L. Zheng, L. Kong, Q. Zhang, C. Y. Zhang, Q. G. Zhang, S. Brovelli and L. Li, *Nat. Photonics*, 2021, **15**, 379–385.

19 J. J. Lou, B. Cai, Y. H. Wu, Y. H. Lv, X. H. Liu, W. H. Zhang and Y. Qin, *J. Alloys Compd.*, 2021, **872**, 159601.

20 Y. Q. Ji, M. Q. Wang, Z. Yang, H. Wang, M. A. Padhiar, J. D. Shi, H. W. Qu and A. S. Bhatti, *J. Phys. Chem. C*, 2022, **126**, 1542–1551.

21 J. D. Shi, W. Y. Ge, J. F. Zhu, M. Saruyama and T. Teranishi, *ACS Appl. Nano Mater.*, 2020, **3**, 7563–7571.

22 W. Y. Ge, J. D. Shi, Y. Tian, M. M. Xu, Y. T. Wu and Y. X. Li, *J. Alloys Compd.*, 2021, **865**, 158768.

23 Q. X. Zhong, M. H. Cao, Y. F. Xu, P. L. Li, Y. Zhang, H. C. Hu, D. Yang, Y. Xu, L. Wang, Y. Y. Li, X. H. Zhang and Q. Zhang, *Nano Lett.*, 2019, **19**, 4151–4157.

24 M. Imran, P. Ijaz, D. Baranov, L. Goldoni, U. Petralanda, Q. Akkerman, A. L. Abdelhady, M. Prato, P. Bianchini, I. Infante and L. Manna, *Nano Lett.*, 2018, **18**, 7822–7831.

25 A. Ray, D. Maggioni, D. Baranov, Z. Y. Dang, M. Prato, Q. A. Akkerman, L. Goldoni, E. Caneva, L. Manna and A. L. Abdelhady, *Chem. Mater.*, 2019, **31**, 7761–7769.

26 C. Roda, A. L. Abdelhady, J. Shams, M. Lorenzon, V. Pinchetti, M. Gandini, F. Meinardi, L. Manna and S. Brovelli, *Nanoscale*, 2019, **11**, 7613–7623.

27 J. S. Chen, P. Chabera, T. Pascher, M. E. Messing, R. Schaller, S. Canton, K. B. Zheng and T. Pullerits, *J. Phys. Chem. Lett.*, 2017, **8**, 5119–5124.

28 J. D. Shi, M. Q. Wang, C. Zhang, J. N. Wang, Y. Zhou, Y. L. Xu and N. V. Gaponenko, *J. Mater. Chem. C*, 2023, **11**, 4742–4752.

29 L. Protesescu, S. Yakunin, M. I. Bodnarchuk, F. Krieg, R. Caputo, C. H. Hendon, R. X. Yang, A. Walsh and M. V. Kovalenko, *Nano Lett.*, 2015, **15**, 3692–3696.

30 H. C. Cho, S. H. Jeong, M. H. Park, Y. H. Kim, C. Wolf, C. L. Lee, J. H. Heo, A. Sadhanala, N. Myoung, S. Yoo, S. H. Im, R. H. Friend and T. W. Lee, *Science*, 2015, **350**, 1222–1225.

31 D. Shi, V. Adinolfi, R. Comin, M. J. Yuan, E. Alarousu, A. Buin, Y. Chen, S. Hoogland, A. Rothenberger, K. Katsiev, Y. Losovyj, X. Zhang, P. A. Dowben, O. F. Mohammed, E. H. Sargent and O. M. Bakr, *Science*, 2015, **347**, 519–522.

32 M. Bruzzi, F. Gabelloni, N. Calisi, S. Caporali and A. Vinattieri, *Nanomaterials*, 2019, **9**, 177.

33 K. J. Babu, G. Kaur, A. Shukla, R. Saha, A. Kaur, M. Sachdeva, D. K. Yadav and H. N. Ghosh, *ACS Photonics*, 2022, **9**, 969–978.

34 C. D. Pu, H. Y. Qin, Y. Gao, J. H. Zhou, P. Wang and X. G. Peng, *J. Am. Chem. Soc.*, 2017, **139**, 3302–3311.

35 W. Z. Lv, L. Li, M. C. Xu, J. X. Hong, X. X. Tang, L. G. Xu, Y. H. Wu, R. Zhu, R. F. Chen and W. Huang, *Adv. Mater.*, 2019, **31**, 1900682.

36 A. D. Wright, C. Verdi, R. L. Milot, G. E. Eperon, M. A. Perez-Osorio, H. J. Snaith, F. Giustino, M. B. Johnston and L. M. Herz, *Nat. Commun.*, 2016, **7**, 11755.

37 J. M. Frost, K. T. Butler, F. Brivio, C. H. Hendon, M. van Schilfgaarde and A. Walsh, *Nano Lett.*, 2014, **14**, 2584–2590.

38 F. Zhang, H. Z. Zhong, C. Chen, X. G. Wu, X. M. Hu, H. L. Huang, J. B. Han, B. S. Zou and Y. P. Dong, *ACS Nano*, 2015, **9**, 4533–4542.

39 Y. Z. Zhu, Q. N. Cui, J. P. Chen, F. Chen, Z. L. Shi, X. W. Zhao and C. X. Xu, *ACS Appl. Mater. Interfaces*, 2021, **13**, 6820–6829.

40 H. D. Jin, E. Debroye, M. Keshavarz, I. G. Scheblykin, M. B. J. Roeffaers, J. Hofkens and J. A. Steele, *Mater. Horiz.*, 2020, **7**, 397–410.

41 Y. M. Zhao, C. Riemersma, F. Pietra, R. Koole, C. D. Donega and A. Meijerink, *ACS Nano*, 2012, **6**, 9058–9067.

42 G. Almeida, L. Goldoni, Q. Akkerman, Z. Y. Dang, A. H. Khan, S. Marras, I. Moreels and L. Manna, *ACS Nano*, 2018, **12**, 1704–1711.

43 E. V. Kolobkova, R. Semaan, M. S. Kuznetsova and N. V. Nikonorov, *J. Lumin.*, 2023, **255**, 119541.

44 X. Y. Zhang, X. Bai, H. Wu, X. T. Zhang, C. Sun, Y. Zhang, W. Zhang, W. T. Zheng, W. W. Yu and A. L. Rogach, *Angew. Chem., Int. Ed.*, 2018, **57**, 3337–3342.